Rare Metal Materials and Engineering
Volume 52, Issue 4, April 2023
Available online at www.rmme.ac.cn

Science Press

Cite this article as: Feng Yinghao, Sun Chaoyang, Xu Sinuo, et al. Hot Workability of Dual-Phase Mg-Li Alloy with $\alpha \rightarrow \beta$ Transformation at Elevated Temperatures[J]. Rare Metal Materials and Engineering, 2023, 52(04): 1227-1237.

ARTICLE

Hot Workability of Dual-Phase Mg-Li Alloy with $\alpha \rightarrow \beta$ Transformation at Elevated Temperatures

Feng Yinghao[1,2], Sun Chaoyang[1,2], Xu Sinuo[1,2], Zhu Nanyang[1,2], Wang Qinglei[1,2], Wang Chunhui[1,2]

[1] School of Mechanical Engineering, University of Science and Technology Beijing, Beijing 100083, China; [2] Beijing Key Laboratory of Lightweight Metal Forming, Beijing 100083, China

Abstract: Hot workability, microstructure evolution, and phase composition of dual-phase Mg-Li alloy were investigated via hot compression test at 250–400 °C with strain rates of 0.1–10 s^{-1}. The optimum hot workability window integrating processing and α-Mg content maps was established. Results show that the established Arrhenius constitutive model can accurately predict the stress flow behavior during work softening. In addition, the microstructure of the alloy shows that dynamic recovery (DRV), dynamic recrystallization (DRX) and α-Mg phase transformation are the main softening mechanisms. α-Mg phase is transformed into β-Li phase in forms of both spheroidization and internal precipitation of α-Mg phase, especially above 300 °C. Meanwhile, the DRX process can easily occur in β-Li phase, whereas in the α-Mg phase it is retarded. Based on the dynamic materials model and microstructure analysis, the optimal processing window can be obtained as 300–350 °C/0.1–1 s^{-1} and 250 °C/0.1 s^{-1}.

Key words: Mg-Li alloy; hot deformation behavior; dynamic recrystallization; workability optimization; phase transformation

Mg-Li alloy, as the lightest metal structural material (1.35–1.65 g/cm^3), is one of the research hotspots due to its low density, excellent electromagnetic shielding, high specific strength and stiffness, etc[1–3]. Furthermore, it is also the potential candidate for structural materials in fields of aerospace, military and 3C industry production, etc[4–7]. However, the relatively low absolute strength is the main drawback of Mg-Li alloys, which restricts their extensive applications. To overcome this drawback, the mechanical properties of Mg-Li alloys need further improvement. Generally, the improvement of material strength is at the expense of its ductility[8]. Accordingly, achieving a combination improvement of strength and toughness of Mg-Li alloys is the key problem for engineering applications. According to Mg-Li alloy binary phase diagram[4, 9], it exhibits different phase compositions with different Li contents: α-Mg single phase (<5.7wt%), α-Mg and β-Li dual-phase (5.7wt%–10.3wt%), and β-Li single phase (>10.3wt%). As is known to all, dual-phase structure is beneficial to balance the strength and ductility. Therefore, the strength and ductility of Mg-Li alloy can be effectively controlled by the dual-phase structure.

Up to now, there are a lot of reports on the microstructure and mechanical properties of Mg-Li alloys, including single or dual-phase alloys[4, 10]. Plastic processing is a common and effective process for fabricating Mg-Li alloys and improving its strength by refining grain and uniform microstructure[9]. Zhou et al[11] fabricated the Mg-7Li-2Al-1.5Sn alloys (dual-phase) by casting and extruding. The results showed that its ultimate tensile strength can be upped from 164 MPa for as-cast state to 324 MPa after extruding and indicated that grain boundary strengthening is the most dominant mechanism. The microstructure and mechanical properties are affected by the plastic deformation parameters significantly, because Mg-Li alloys are very sensitive to the deformation temperature[12]. Accordingly, research on hot deformation behavior is very important for the metal forming process, in which constitutive models and hot processing map have been widely used to guide material processing. Wei et al[13] established three kinds

Received date: September 21, 2022
Foundation item: National Natural Science Foundation of China (52175285, 52161145407); Fundamental Research Funds for the Central Universities (FRF-BD-20-08A, FRF-AT-20-09, FRF-TP-20-009A2)
Corresponding author: Sun Chaoyang, Ph. D., Professor, University of Science and Technology Beijing, Beijing 100083, P. R. China, Tel: 0086-10-62332261, E-mail: suncy@ustb.edu.cn

of models, i.e. Ludwik, Zener-Hollomon and modified Hensel-Spittel models, to evaluate their ability in accurately predicting the constitutive behavior and the results showed that the Zener-Hollomon models show a good agreement between calculated and measured flow stress during work softening. Yang et al[10] described the flow behavior of Mg-9Li-3Al-2.5Sr alloy accurately by hyperbolic sine function, and suggested the optimum hot working conditions by processing map which corresponds to the dynamic recrystallization (DRX) region. Shalbafi et al[14] studied the hot deformation behavior of Mg-10Li-1Zn alloy (LZ101) by compression testing. By comparing experimental and predicted stress-strain data calculated by Arrhenius constitutive equation, the root mean square error is about 2 MPa, indicating that the accuracy of the Arrhenius-type constitutive equation is quite acceptable.

In general, Mg alloys are the low stacking fault energy (SFE) materials[15]. But the β-Li phase is the body centered cubic (bcc) structure which has high SFE[16]. Meanwhile, the SFE increases with the increase in Li content[4]. Different SFE will lead to different mechanisms, especially for dual-phase Mg-Li alloys. There are some reports about softening mechanism of single and dual-phase alloys. Sun et al[15] fabricated Mg-xLi-3Al-2Zn-0.2Zr (x=5, 7, 8, 9, 11, wt%) alloys by vacuum melting, and studied the DRX mechanisms of α-Mg and β-Li phase after extruding, which undergoes discontinuous DRX (DDRX) and continuous DRX (CDRX), respectively. Li et al[9] investigated the hot deformation mechanism and microstructure evolution of Mg-5Li-3Al-2Zn (single α phase) alloy. The DRX mechanism can be considered to be DDRX. Xu et al[17] investigated the DRX behavior of as-cast Mg-9.15Li-3.23Al-1.18Nd alloy and results showed that the DRX can easily occur in β-Li phase, but the DRX in α-Mg phase will be restrained.

In order to clarify the hot deformation mechanism and optimal processing window of dual-phase Mg-Li alloy, in this study, hot deformation behavior and microstructure evolution of LA103Z were studied by compression testing. Meanwhile, the mechanism of α-Mg phase transformation was revealed. Finally, the optimum hot processing window was established by integrating the processing map with α-Mg content maps and analyzing the microstructure evolution. The study on hot deformation characteristics is expected to contribute to the hot deformation of high-performance Mg-Li alloys.

1 Experiment

The raw material employed in this research was commercial as-extruded LA103Z magnesium-lithium alloy which was provided by Xi'an Sifang Ultralight Material Co., Ltd. The main chemical composition of LA103Z is shown in Table 1. The compression specimens were machined into a cylinder with 8 mm in diameter and 10 mm in height and their axes are aligned along the extrusion direction (ED). The surface of specimens was polished by 1500# sandpaper slightly in order to eliminate surface defects. Uniaxial hot compression tests were carried out on a Gleeble-1500 thermal simulation testing machine at different temperatures (250, 300, 350, and 400 °C) and different strain rates (0.1, 1 and 10 s^{-1}). The compression direction (CD) was parallel to the ED and the compression tests were conducted to a final true strain of 0.7. Before compression, thermocouple wires used for heating and temperature measurement were welded to the longitudinal midpoint of the specimen. Graphite flakes were attached to the terminal surfaces of the specimen to reduce the friction. The specimens were heated to the aim temperature at 5 °C/s and then held isothermally for 1 min before loading. After deformation, all specimens were quenched by water to freeze the deformation microstructure.

Table 1 Chemical composition of commercial LA103Z Mg-Li alloy (wt%)

Li	Al	Zn	Si	Fe	Cu	Mg
10.0	3.2	2.8	0.05	0.05	0.05	Bal.

The deformed specimens were cut in half along the CD for microstructure and texture investigation. And then the cut surfaces were polished and etched (by 4% nitric alcohol) for metallographic analyses by optical microscopy (OM). The phase constitution was analyzed by X-ray diffraction (XRD, RIGAKU D/max-RB), and the specific parameters were as follows: Cu target, voltage of 40 kV, current of 100 mA, scanning range of 10° – 90° and scanning speed of 4°/min. Scanning electron microscopy (SEM, SU5000) was used to observe the grain size and microstructure. Image J software was used to count the phase content.

2 Results and Discussion

2.1 Initial microstructure and phase composition

Fig. 1 shows the XRD patterns of the commercial LA103Z alloy sample and hot compressed specimens in the strain rate of 0.1, 1, and 10 s^{-1} and temperature of 250, 300, 350, and 400 °C. It is confirmed that all LA103Z alloy specimens are the typical solid-solution alloy which is mainly composed of α-Mg and β-Li phases, as well as $MgAlLi_2$ and AlLi minor phases. The result is consistent with the phase diagram[18] and other reports[8,15], when Li content is in a range of 5.7wt% – 10.3wt%. There is an obvious transformation, i.e. the intensity of β-Li diffraction peak increases and α-Mg peak decreases as the temperature rises inside the black dashed box. The results

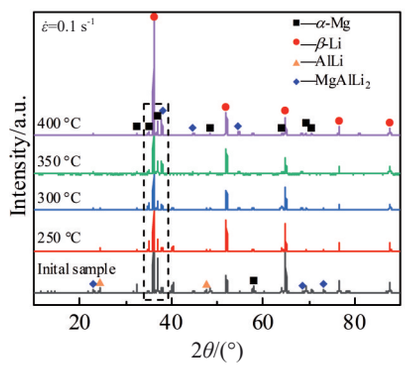

Fig.1 XRD patterns of LA103Z alloy samples

indicate that elevated working temperature can promote phase transformation from α-Mg phase to β-Li phase.

In Fig. 2a, equiaxed β-Li phases in gray color, rod-like and globular α-Mg in white color are observed, the average grain size of β -Li and α -Mg phases is 9.52 and 21.2 μm, respectively, and the area fraction of α -Mg phases is approximately 19.21%. Meanwhile, a few big white particles and little precipitate phase in the grain boundary are observed in Fig. 2a and 2b. A combination of XRD and EDS clarifies that the former is AlLi phase and the latter is $MgAlLi_2$ phase. According to Qu's report[19], bright particles are AlLi compounds and the smaller size particles and lamellar should be AlLi and $MgAlLi_2$ in as-cast LA96 alloy.

2.2 Hot compression flow stress-strain behavior

Fig. 3 shows the true stress-strain curves at temperatures of 250, 300, 350, and 400 °C and strain rates of 0.1, 1, and 1 s^{-1}. Similar to most magnesium alloys, the true stress-strain curve of LA103Z plastic deformation part can be divided into three stages: work hardening, dynamic softening and steady state.

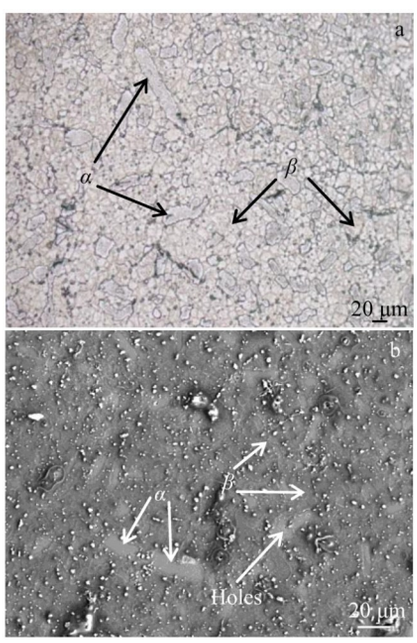

Fig.2 OM image (a) and SEM morphology (b) of initial sample

After elastic deformation, work hardening is the leading mechanism until true stress reaches the peak, which is attributed to the dislocation multiplication, pile up, tangling or twin formation[10]. As the deformation continues, the dislocation density increases, and the driving force of dynamic recovery (DRV) and DRX increases. Eventually, the flow stress reaches a steady state due to the balance between hardening and softening. As shown in Fig. 3b, there are two types of curves due to different softening mechanisms. Once over the peak stress, the flow stress decreases as softening mechanisms to overcome work hardening, which is a typical characteristic of DRX[20]. It is worth noting that there is no peak stress curve appearance at the strain rate of 0.1 s^{-1}, especially at 250 ° C, which shows the characteristic of DRV[21]. Askariani[22] and Zhou[23] reported that there is no peak behavior in the stress-strain curves and reasoned the introduction of the DRV during the hot compression. Therefore, it is believed that the preferred softening mechanism of Mg-Li alloys is determined by hot working parameters.

The flow stress presents decrease trend with increasing temperature and decreasing strain rate (at a given strain rate or temperature), which indicates that the flow stress has a strong temperature sensitivity and strain rate sensitivity. As the temperature increases, the decrease in flow stress is attributed to high mobility of dislocations and grain boundaries, and rearrangement and annihilation of dislocation caused by the improvement of vacancy diffusivity at elevated temperatures. Meanwhile, the flow stress decrease caused by the shear stress is declined and grain boundaries slide more easily, because the thermal activation of atoms is enhanced and the binding force between atoms is weakened as the temperature increases[9]. In addition, the content of α-Mg phase significantly declines at elevated temperatures, and the bcc (β-Li phase) lattice has more operative slip system and lower strength than hcp (α-Mg phase) lattice, which is one of the reasons for flow stress decrease as the temperature rises[24]. At low strain rates, there is sufficient time for dislocation annihilation and softening of DRV and DRX.

It is worth noting that the curves exhibit oscillations at the strain rate of 0.1 s^{-1}, which can be explained by the following reasons. Wang[25] regarded this phenomenon as discontinuous

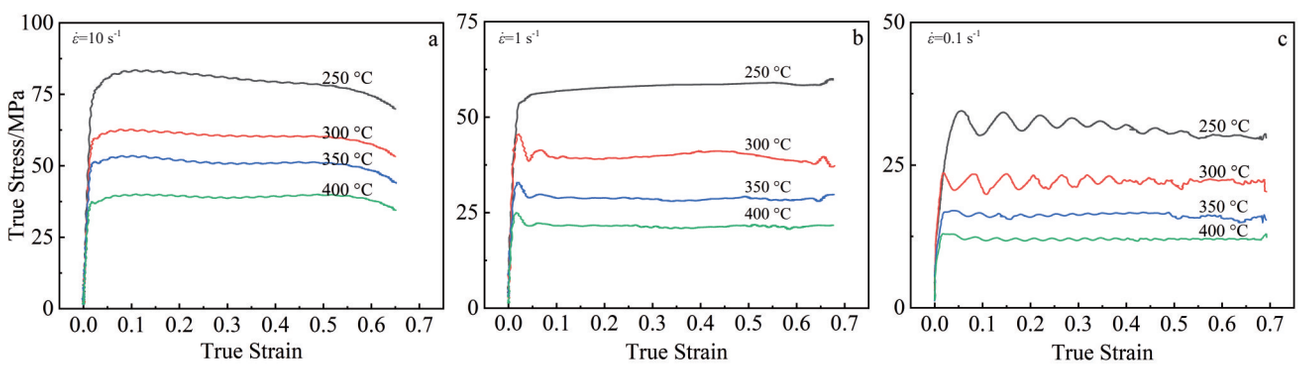

Fig.3 True stress-strain curves of LA103Z alloy at different temperatures and strain rates: (a) 10 s^{-1}, (b) 1 s^{-1}, and (c) 0.1 s^{-1}

yielding, and ascribed it to the generation of new mobile dislocation at the grain boundary, which was proved through the transmission electron microscope observation. Besides, DRX grains not only have nucleation and growth process, but also deform for coarse DRX grains as the strain increases, and transform to secondary DRX. The new secondary DRX grains also undergo a process of growing, hardening and softening. Consequently, the stress-strain curve may present multiple peaks periodically[26]. Some reports suggest that flow instability and dissolution and precipitation of secondary particles can cause the curve oscillations during hot deformation[27].

2.3 Basic constitutive equation

Understanding the behavior of materials for optimizing processing parameters is of great importance. It is generally thought that the flow behavior of Mg alloys can be described by a relation between processing parameters such as temperature (T), stress (σ), strain (ε), and strain rate ($\dot{\varepsilon}$). The hot deformation of metal materials is a process of heat collection activation control. Arrhenius equation is used for properly capturing the work softening behavior of the material during deformation with hyperbolic sine law, which has been broadly used[3]. Arrhenius constitutive equation can be expressed as follows[28–30]:

$$\dot{\varepsilon} = A_1\sigma^{n_1}\exp\left(\frac{-Q}{RT}\right) \quad (1)$$

$$\dot{\varepsilon} = A_2\exp(\beta\sigma)\exp\left(\frac{-Q}{RT}\right) \quad (2)$$

$$\dot{\varepsilon} = A[\sinh(\alpha\sigma)]^n\exp\left(\frac{-Q}{RT}\right) \quad (3)$$

where A_1, A_2, A, n_1, n, β (MPa^{-1}), and α ($\alpha=\beta/n_1$, MPa^{-1}) are materials constant, $\dot{\varepsilon}$ (s^{-1}) is strain rate, σ (MPa) is the peak stress, T (K) is the absolute temperature during hot deformation, R is the molar gas constant, and Q (J/mol) is the activation energy. Eq.(1) is applicable at low stress level ($\alpha\sigma$ is less than 0.8), Eq.(2) is suitable for high stress standard ($\alpha\sigma$ is greater than 1.2), while Eq.(3) is suitable for a wide range of stress. Taking the logarithm on both sides of Eq.(1)–Eq.(3) as follows:

$$\ln\dot{\varepsilon} = \begin{cases} \ln A_1 + n_1\ln\sigma - Q/RT \\ \ln A_2 + \beta\sigma - Q/RT \\ \ln A + n\ln[\sinh(\alpha\sigma)] - Q/RT \end{cases} \quad (4)$$

It can be seen from Eq.(4) that there is a linear relationship for ln$\dot{\varepsilon}$-lnσ, ln$\dot{\varepsilon}$-σ, and ln$\dot{\varepsilon}$-ln[sinh($\alpha\sigma$)] at the same temperature. As shown in Fig.4a–4c, in order to obtain the value of n_1, n, and β, the linear fitting calculation of all experimental data is conducted by considering the value of the peak stress. The slopes of patterns for ln$\dot{\varepsilon}$-lnσ, ln$\dot{\varepsilon}$-σ, and ln$\dot{\varepsilon}$- ln[sinh($\alpha\sigma$)] are n_1=4.23, n=3.08, and β=0.12, respectively, and α=0.03 can be calculated by the above mentioned equations. Here n is the stress exponent in the deformation process, which can represent the rate-controlling mechanism. The value of n obtained is 3.08, very close to n=3 as predicted by deformation theories involving dislocation climb as the rate-controlling mechanism, which has been demonstrated by other researchers[31].

In Arrhenius theory, the deformation activation energy describes the energy barrier for the transition of atoms to overcome, which represents the workability of alloys and hot deformation behavior[23, 28]. Deformation activation energy Q is expressed as:

$$Q=Rn\{\partial\ln[\sinh(\alpha\sigma)]/\partial(1/T)\} \quad (5)$$

Q can be measured from the slope of the curve of ln[sinh($\alpha\sigma$)] −1/T at a given strain rate, as shown in Fig. 4d. The average value of Q is 71.18 kJ/mol which is lower than the lattice self-diffusion activation energy of magnesium (135 kJ/mol)[22]. The Q value is lower than that of other Mg-Li alloys, such as as-cast Mg-4.3Li-4.1Zn-1.4Y (147.18 kJ/mol) [23], Mg-5Li-3Al-2Zn (159.8 kJ/mol) [9], Mg-8Li-3Al-2Zn-0.2Zr (107.55 kJ/mol) [32], and Mg-9Li-3Al-2Y (95.45

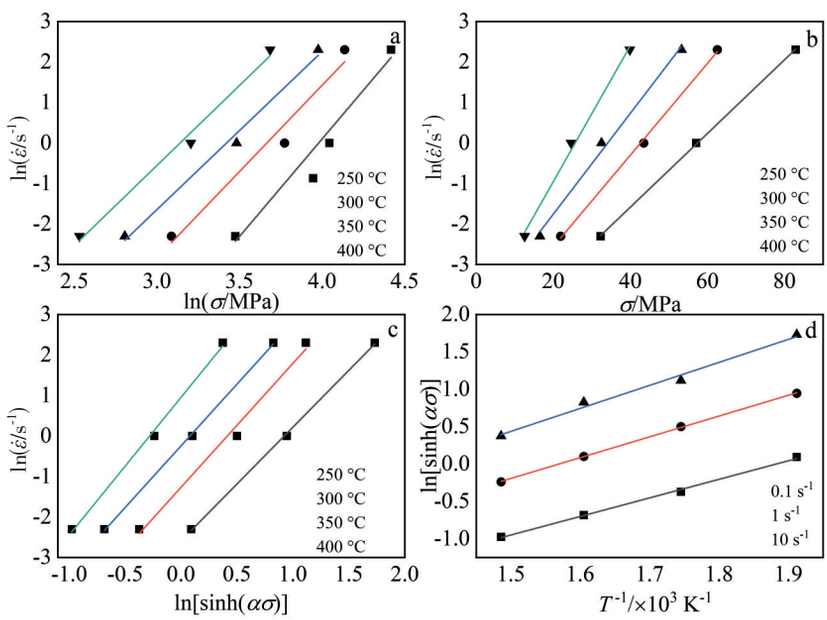

Fig.4 Linear relationship fitting at peak stress: (a) ln$\dot{\varepsilon}$-lnσ, (b) ln$\dot{\varepsilon}$-σ, (c) ln$\dot{\varepsilon}$-ln[sinh($\alpha\sigma$)], and (d) ln[sinh($\alpha\sigma$)]-(1/T)

kJ/mol)[33]. This is mainly due to the existence of softener β-Li phase which can reduce the flow stress of LA103Z alloy compared with single phase alloys. Meanwhile, the axial ratio c/a of lattice decreases as Li element content increases in Mg-Li alloys[2]. The reduction of the axial ratio c/a makes more slip systems easier to be actuated, because of a lower critical resolved shear stress (CRSS), resulting in the decrease in deformation activation energy[9].

Zener-Hollomon (Z) parameter is widely used to describe the relationship between temperature and strain rate. Z parameter is defined by Eq.(6). Taking the logarithm on both sides of Eq.(6) to obtain Eq.(7):

$$Z = \dot{\varepsilon}\exp(Q/RT) = A[\sinh(\alpha\sigma)]^n \quad (6)$$

$$\ln Z = \ln A + n\ln[\sinh(\alpha\sigma)] \quad (7)$$

The relationship between $\ln Z - \ln[\sinh(\alpha\sigma)]$ is plotted and fitted, as shown in Fig.5. The values of $\ln A$ are calculated as 13.57 which is the intercept of the fitting line. According to $\alpha\sigma$, values corresponding to the maximum and minimum peak stress are calculated as 2.4 and 0.36, respectively. Thus, it is inferred that the hyperbolic sine function can describe the constitutive equation of LA103Z alloy appropriately. Substituting the calculated values of Q, A, n, and α, the peak constitutive equation of LA103Z during hot deformation can be expressed as:

$$\dot{\varepsilon} = e^{13.57}[\sinh(0.029344\sigma)]^{3.08}\exp\left(\frac{-71187.7}{RT}\right) \quad (8)$$

In order to accurately describe the flow behavior of LA103Z alloy, the effect of strain is considered. The flow stress data are extracted for the true strain between 0.05 and 0.65 with intervals of 0.05 under all conditions. The value of α, n, Q, $\ln A$ at each strain interval is calculated by Eq.(4)–Eq.(7). The stress exponent n, close to 3, is associated with dislocation slip controlled by solute drag in the overall

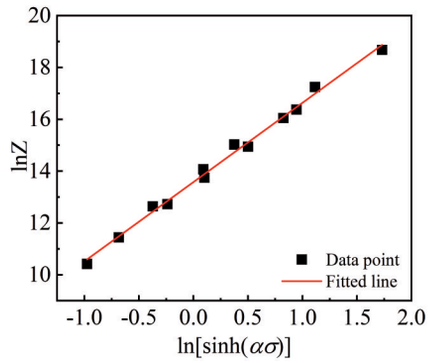

Fig.5 Relationship between $\ln Z - \ln[\sinh(\alpha\sigma)]$

temperature range[34]. The parameters are plotted in Fig.6, and an obvious nonlinear relationship exists. Thus the 6th polynomial curves are plotted and the 6th polynomial Eq.(9) are fitted, in which the correlation coefficient is above 0.99 that presents the influence of strain on material constants with a good correlation.

$$\begin{cases} \alpha = 0.03 - 0.09\varepsilon + 0.89\varepsilon^2 - 4.14\varepsilon^3 \\ \quad +10.04\varepsilon^4 - 12.34\varepsilon^5 + 6.10\varepsilon^6 \\ n = 3.33 - 5.85\varepsilon + 36.44\varepsilon^2 - 71.22\varepsilon^3 \\ \quad -15.03\varepsilon^4 + 165.53\varepsilon^5 - 113.03\varepsilon^6 \\ Q = 68.74 + 93.19\varepsilon - 713.89\varepsilon^2 + 3855.40\varepsilon^3 \\ \quad -10551.68\varepsilon^4 + 12615.03\varepsilon^5 - 5070.29.03\varepsilon^6 \\ \ln A = 13.04 + 26.43\varepsilon - 223.61\varepsilon^2 + 1165.13\varepsilon^3 \\ \quad -3111.41\varepsilon^4 + 3800.28\varepsilon^5 - 1660.61\varepsilon^6 \end{cases} \quad (9)$$

In summary, according to Eq.(3) and Eq.(6), the Zener–Hollomon equation can be expressed as Eq.(10):

$$\sigma = \frac{1}{\alpha}\operatorname{arcsinh}\left[\exp\left(\frac{\ln\dot{\varepsilon} - \ln A + Q/RT}{n}\right)\right] \quad (10)$$

Fig.7 is the comparative distribution diagram between the

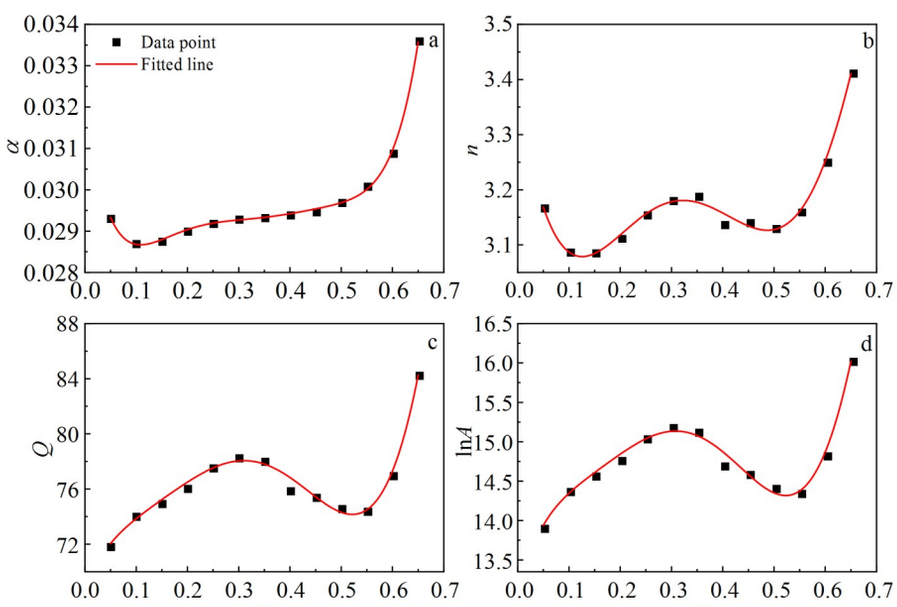

Fig.6 Relationship between true strain and various constants: (a) α, (b) n, (c) Q, and (d) $\ln A$

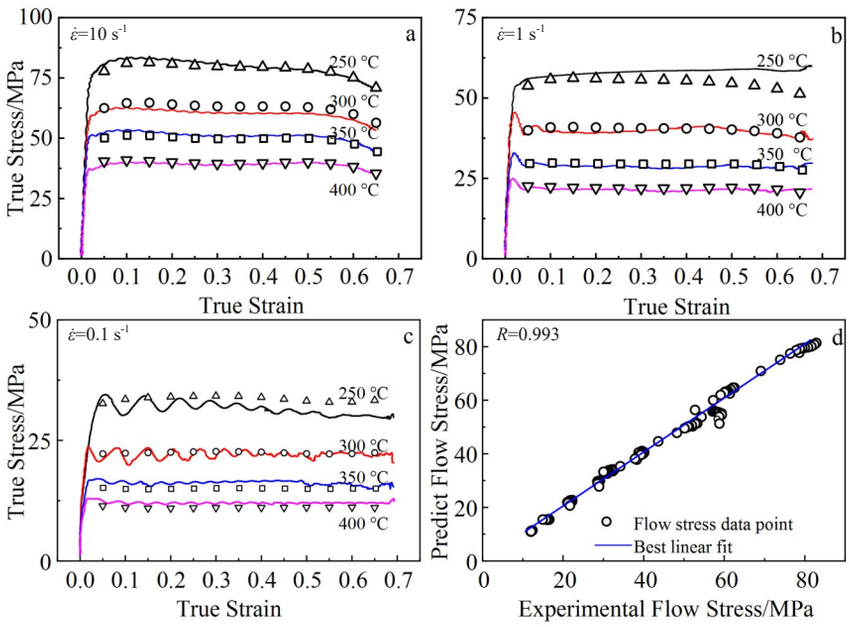

Fig.7 Comparison between predicted values and actual values under different deformation conditions: (a) 10 s^{-1}, (b) 1 s^{-1}, (c) 0.1 s^{-1}; correlation coefficient (d)

experimental curve and the predicted value of the Zener – Hollomon equation under different temperatures and strain rates. The theoretical stress at ε=0.05−0.65 (interval 0.05) is calculated using Eq.(9) and Eq.(10). It can be seen that there is good agreement, and the model can well describe the hot deformation behavior of LA103Z alloy. Fig. 7d shows comparisons of 156 groups of data between the experimental and predicted results. The correlation coefficient R and average relative error AARE are introduced, in order to further verify the accuracy of established constitutive. The values of R and AARE are 0.993 and 3.71%, respectively. The results imply that the established deformation constitutive equation provides an accurate prediction of stress in hot deformation and can be used for deformation calculation.

2.4 Microstructure evolution

Fig. 8 is the optical micrographs of as-extruded samples at

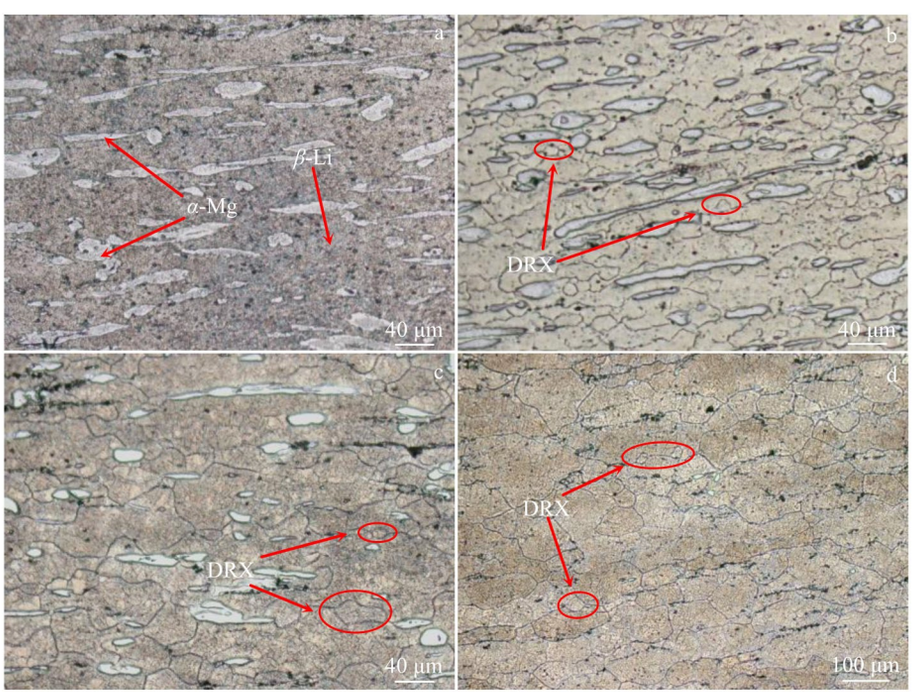

Fig.8 Optical micrographs of deformation samples at strain rate of 0.1 s^{-1} and different temperatures: (a) 250 °C, (b) 300 °C, (c) 350 °C, and (d) 400 °C

strain rate of 0.1 s^{-1} and different temperatures. As shown in Fig.9, there are some visible appearances. In fact, α-Mg phase (white area) is elongated perpendicular to compression direction after compressing, and the α-Mg phase refinement and spheroidization are more obvious with the increasing of deformation temperature. In contrast, the β-Li phase exhibits a relatively higher growth rate than the α-Mg phase, the increase in temperature can increase the mobility of grain boundaries, leading to an increase in the grain sizes of β-Li phase (gray area). Additionally, the area ratio of α-Mg phase decreases significantly with the increase in temperature, especially at 400 °C. The proportion of α-Mg phase is approximately 19.21% in the initial sample, and that of other as-compressed samples is 14.61%, 9.15%, and 4.88% corresponding to 250, 300, and 350 °C, respectively. The content of α-Mg phase at 400 °C is not counted, because it is so small that the statistics are inaccurate. There are some black spots in the optical micrographs which present white particles in Fig. 2b and Fig. 10d. According to the XRD result and other reports[15], it can be confirmed that the particles-like and the thread-like phases are AlLi mainly distributed in β-Li phase and $MgAlLi_2$ distributed along the grain boundaries, respectively.

Corresponding to the flow stress-strain curves, DRV and DRX as softening mechanism may take place upon deformation at high temperatures. In Fig. 8b – 8d, the coarse deformed grains and fine grains coexist in the samples, in which the fine grains are distributed at the grain boundaries and trigeminal grain boundaries. The formation of fine grains is due to DRX caused by the local grain boundary migration, which is defined as DDRX. But the amount of DDRX grains of β-Li phase is very little. The same recrystallization

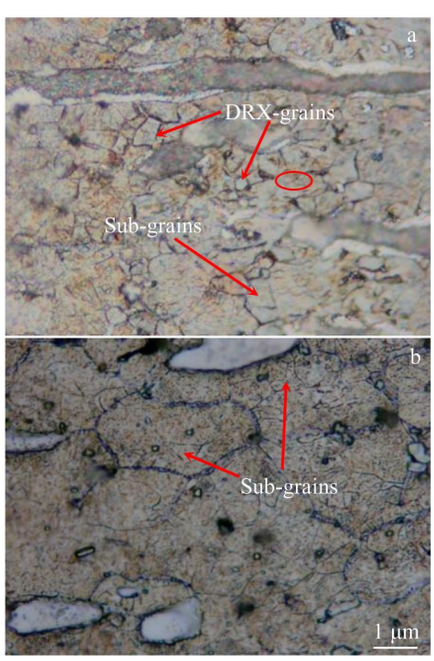

Fig. 9 High magnifications optical micrographs at strain rate of 0.1 s^{-1} and temperature of 250 °C (a) and 350 °C (b)

mechanism of β-Li phase has been reported by Sun[32]. In Fig. 8a, it is hard to find new recrys-tallized grains at 250 °C due to the small grains. High magnifications optical micrographs (Fig.9a) shows a lot of DRX grains, and the same recrystallization mechanism is reported at Li's research[35]. This phenomenon can be interpreted by the fact that β-Li phase has a high SFE which is the bcc crystal and has been reported[16,36]. For high SFE alloys, DRV is likely to occur since the narrow extended dislocations are easily concentrated and dislocations move more easily for cross slip and climb during the hot deformation[37]. Meanwhile, the annihilation and rearrangement of dislocations form a large number of sub-grains in the grains. Thus, a lot of sub-grains and low angle grain boundaries can be observed in Fig. 9. At larger strain, with the accumulation of energy and dislocation, the DRX will be achieved by the transformation from low angle grain boundaries into high angle grain boundaries, and this mechanism is termed as CDRX[38]. The strength of β-Li phase is lower than that of α-Mg phase, and the plastic deformation first occurs in β-Li phase. Thus, DRX of α-Mg phase is restrained, because the driving force of DRX and dislocation density of α-Mg phase are reduced by the DRV and DRX of β-Li phase[32].

As shown in Fig. 10, α-Mg phase appears in β-Li phases which is marked by the yellow dashed box. This is a phase transformation process as new β-Li phase replaces the prior α-Mg phase, until the prior α-Mg phase is completely separated. In Guo's report[39], the grain boundaries and sub-grain boundaries in α-Mg phase are the nucleation sites of β-Li phase. Meanwhile, it is illustrated that the small holes in α-Mg phase is a sign of the nucleation of β-Li phase. Similarly, initial samples have some holes in α-Mg phase in Fig.2b. Mg-Li alloy is the solid solution alloy, atomic diffusion rate of Li is faster than that of Mg at the same temperature[3]. Thus, Li atoms can easily diffuse to the nucleation site of α-Mg phase, which causes poor Li in α-Mg phase. According to the Mg-Li binary phase diagram and the lever rule, it is β-Li phase when the solid solubility of Li reaches 11.3wt%. Consequently, high Li concentration meets the requirement for phase transformation kinetics, and phase transformation is conducted. The β-Li phase in α-Mg phase grows gradually because of the phase boundary migration as the deformation processes. Meanwhile, the phase transformation is one of the reasons for the decrease in content of β-Li phase and size of β-Li phase.

It is believed that the spheroidization of α-Mg phase is also a softening mechanism which is a result of atomic diffusion[32]. As shown in Fig. 10, the serrated boundaries of elongated α-Mg phases exist, especially in the red dashed box. And the spheroidization of α-Mg phase is more pronounced at elevated temperatures, because high temperature is beneficial to atomic diffusion. Meanwhile, it can be inferred that the spheroidization of α-Mg phase is a result of phase boundary migration[39]. This mechanism is also reported in Ti alloys. Zhang et al[40] indicated that with the continuous deformation, the strain concentration in the concave may cause the shear stress, which can promote the migration of phase boundary

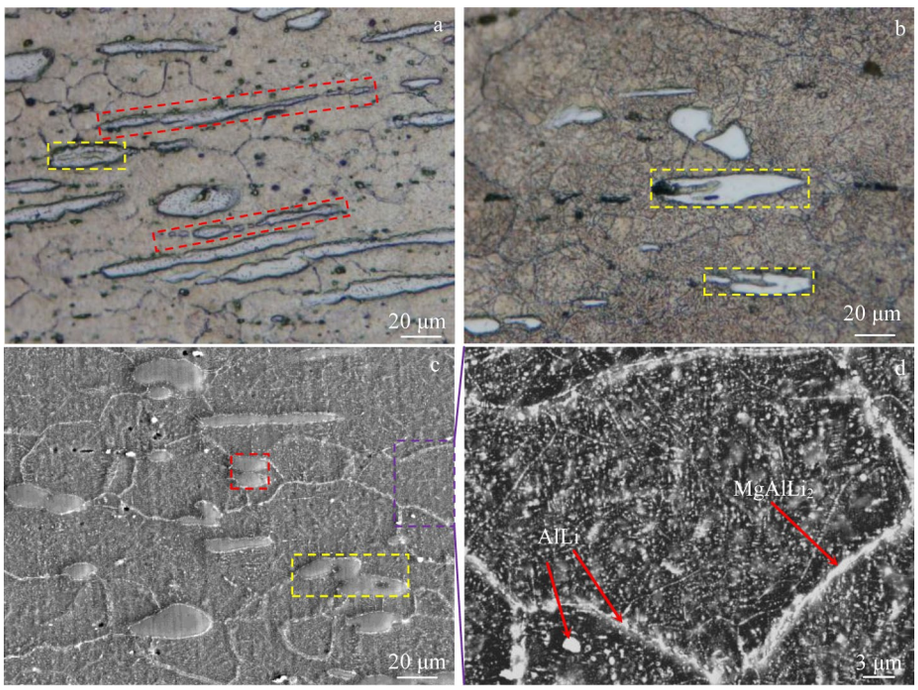

Fig.10 Optical (a, b) and SEM (c, d) micrographs of deformation samples at strain rate of 0.1 s^{-1} and different temperatures: (a) 300 °C, (b) 350 °C, and (c, d) 350 °C

until the α-Mg phase is broken. This is another reason for phase transformation and the decrease in β-Li phase size. In short, the reasonable distribution of two phases content according to processing parameters is also an important approach to control the balance of strengthening and toughening of Mg-Li alloys.

Fig.10d is the partially-enlarged view of Fig.10c. According to the phase evolution of LA103Z in XRD pattern, it can be found that the content of blocky AlLi phase decreases significantly, and the content of threadlike $MgAlLi_2$ at the grain boundary increases as deformation temperature rises, especially in Fig. 2b and Fig. 10d. Simultaneously, there are small spheric particles which may be precipitated from matrix during aging at room temperature[19]. Similar to Ref. [15, 41], $MgAlLi_2$ is precipitated from β-Li phase during the hot processing and heat treatment, while the AlLi phase is dissolved into matrix. Generally, secondary particles will cause the dislocation pile up and arranging, so dislocation storing increases in local area, and the driving force for recrystallization increases. Moreover, the growth of recrystallized grains is attributed to the mobility of grain boundaries, so the growth of recrystallized grains will be inhibited by secondary particles.

The content of α-Mg phase is counted quantitatively at different compression parameters, as shown in Fig. 11. The content of α-Mg phase at 400 °C is not counted, since there is few α-Mg phase, almost 0%. It can be seen that α-Mg phase content decreases considerably as the temperature rises and is also affected by strain rate but it is not obvious. Thus, it can be referred that α-Mg phase content is highly sensitive to temperature.

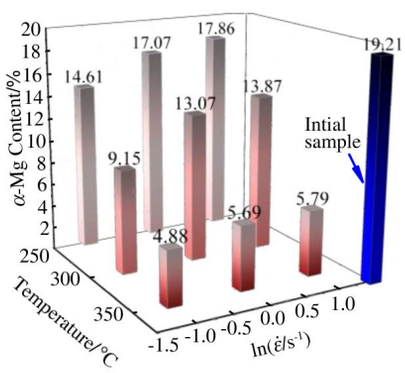

Fig.11 Content of α-Mg phase at different compression parameters

2.5 Hot workability and phase transformation

Hot processing map is usually used to describe the hot workability of materials and to optimize process variables. Processing map based on dynamic material model (DMM) has been successfully applied for various materials[10]. It is the superposition of power dissipation map, which reflects the power dissipation caused by microstructure evolution in the process of deformation, and instability map, which designates the stability and instability region[42]. According to the DMM, the instantaneous absorbed power per unit volume of material is the product of stress and strain rate, in the process of hot working. The total power P contains two parts: G, the energy dissipated through plastic deformation, and J, the energy dissipated through microstructure evolution, which can be expressed as Eq.(11):

$$P = \sigma\dot{\varepsilon} = G + J = \int_0^{\dot{\varepsilon}} \sigma \mathrm{d}\dot{\varepsilon} + \int_0^{\sigma} \dot{\varepsilon} \mathrm{d}\sigma \quad (11)$$

The strain rate sensitivity coefficient m is believed as the distribution coefficient of two parts energy J and G[14]. It is expressed as Eq.(12):

$$\frac{\mathrm{d}J}{\mathrm{d}G}=\frac{\dot{\varepsilon}\mathrm{d}\sigma}{\sigma\mathrm{d}\dot{\varepsilon}}=\frac{\partial\ln\sigma}{\partial\ln\dot{\varepsilon}}=m \tag{12}$$

Maximum value of J is obtained at m=1, and $J_{max}=\sigma\dot{\varepsilon}/2=P/2$. The power dissipation efficiency η reflects the relationship between the energy dissipated through microstructure evolution and the total dissipated energy power, expressed as Eq.(13):

$$\eta=\frac{J}{J_{max}}=\frac{2m}{m+1} \tag{13}$$

The dissipation map is plotted as the strain rate-temperature contour map. The value of contour represents the efficiency of the energy dissipated through microstructure evolution corresponding to the softening mechanism at different deformation parameters. The higher the η value, the larger the driving force for grain boundaries and dislocation. But the dissipation map is unable to specify safe and unsafe regions. Flow instability caused by defects such as cracking, hole and adiabatic shear bands also exists in the process of deformation, because of the unreasonable processing parameters.

According to Prasad instability criterion[43], the continuum instability ξ criterion is expressed as Eq.(14):

$$\xi(\dot{\varepsilon})=\frac{\partial\ln[m/(m+1)]}{\partial\ln\dot{\varepsilon}}+m<0 \tag{14}$$

Instability map is constructed with different deformation conditions and can be divided into two parts: instability region with negative value of ξ and safe region with positive value of ξ.

Fig.12 shows the processing maps corresponding to the true strain of 0.3 and 0.7. There is an instability region (red shaded area) and a stable power dissipation region under the processing maps. At a true strain of 0.3, it can be seen that the instability domain is mainly concentrated under the condition of low temperature and low strain rate (250 °C, $\dot{\varepsilon}$ is greater than 1 s^{-1}; 300 °C, $\dot{\varepsilon}$ is greater than 10 s^{-1}). At a true strain of 0.7, the area of instability domain (250–300 °C, $\dot{\varepsilon}$ is greater than 1 s^{-1}) increases clearly. Thus, it indicates that the instability domain expands to a moderate strain rate and middle temperature region with increasing strain. The reason is that the recovery mechanism is not fast enough to reduce the stress concentration when the strain increases.

The processing map can be divided into two main domains in Fig.12b. In order to obtain the optimum processing region, the workability of the alloy in each domain is discussed with the help of the deformed microstructure. It can be seen from domain 1 (instability region) in Fig. 12b that the instable region shows local flow characteristics, and some grain edges show shear state. Shear bands will occur as the strain increases. In addition, the power dissipation efficiency increases gradually, with the increase in deformation temperature and the decrease in instrain rate. In general, the high power dissipation coefficient corresponds to the optimum processing conditions, and it is termed as domain 2 in this study. Microstructure presents homogeneous and DRX structures without deformation defect at 300–350 °C/0.1–1 s^{-1} and 250 ° C/0.1 s^{-1}. When the deformation temperature is 400 ° C, although there are relatively uniform grains, the microstructure exhibits extraordinary grain growth behavior, i.e. most grain sizes reach up to 100 μm. Meanwhile, there is almost no α-Mg phase, which is the strengthening phase. Thus, the strength of samples at deformation condition of 400 °C will decrease significantly.

Here, we try to elucidate the possible mechanism for α-Mg phase transformation. Fig. 13a is the schematic diagram of

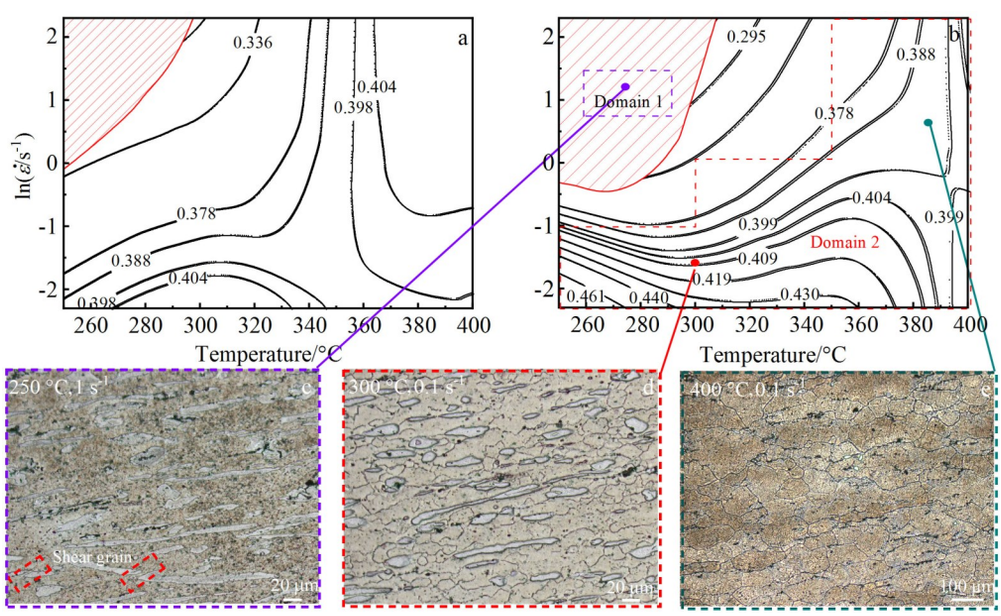

Fig.12 Hot processing maps of LA103Z alloy at a true strain of 0.3 (a) and 0.7 (b) and optical micrographs corresponding to domain 1 (c) and domain 2 (d, e) marked in Fig.12b

transformation mechanisms from α-Mg phase to β-Li phase. At elevated temperature, both the mutual diffusion rate and solid solubility of Mg and Li increase[44], phase boundary migration (from β-Li phase to α-Mg phase) will be intensified in Mg-Li alloys dominated by Li phase. This will also result in the formation of supersaturated β-Li phase, and quenching can retain the supersaturated solid solution structure. During the compression, the mechanism of phase boundary migration occurs in two forms as the strain increases. The one is that β-Li phase is precipitated at grain boundary and sub-grain boundary inside α-Mg phase which is marked by black circle. The other is phase boundaries migration and the spheroidization of α-Mg phase. Geometric DRX (GDRX) has been commonly described as follows (Fig.13): (a) the original grains are flattened or elongated, and the high angle grain boundaries migrate to form serrations; (b) when the thickness of the original grain approaches twice the diameter of the sub-grain, the serrated grain boundaries begin to contact each other until the original grains are divided[38]. GDRX commonly form in deformation of high temperature and strain, especially under the condition of inhomogeneous deformation. In dual-phase Mg-Li alloys, inhomogeneous deformation is easy to occur due to the obvious difference in strength of the two phases. Thus, the spheroidization of α-Mg phase may be thought as GDRX. As shown in Fig. 13b, the degree of transformation will be more intense and the content of α-Mg phase will decrease based on the above mechanisms as the deformation temperature increases.

Fig. 14 is the hot processing window at a strain of 0.7, which is coupled with the contour map for α-Mg phase content (represented by blue contour). The blue arrows mark the trend of α-Mg phase content as the parameters vary. Based on the above discoveries, the microstructure of LA103Z Mg-Li alloy is sensitive to temperature, especially the grain size of β-Li and phase composition. The hot working window can be divided into four main regions: flow instability region, partial DRX region, processing region, and single phase region. Through comprehensive analysis of hot processing maps, phase composition and microstructure of LA103Z Mg-Li alloy at a strain of 0.7, the workable regions, i.e. 300–350 °C/0.1–1 s^{-1} and 250 °C/0.1 s^{-1}, are thought optimal, which are

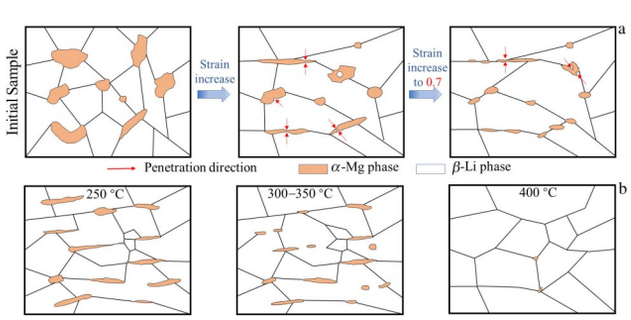

Fig.13 Schematic diagrams of α-Mg phase transformation mechanisms (a) and α-Mg phase evolution at different deformation temperatures (b)

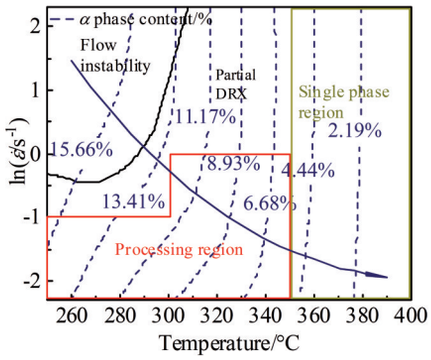

Fig.14 Hot processing window of coupling α-Mg phase content at a strain of 0.7

characterized by relatively homogeneous grains, low deformation resistance and high machining efficiency. Thus, it is recommended as the optimal workable range for LA103Z Mg-Li alloy. Actually, processing parameters can be further selected according to the actual conditions, such as forming load and processing efficiency.

3 Conclusions

1) The flow stress of LA103Z alloy shows the typical characteristic of DRX, and the characteristic of DRV at lower temperatures and lower strain rate. The stress exponent is close to 3, and rate control mechanism is suggested as dislocation slip controlled by solute drag.

2) The grain size of β-Li has a visible growth as the temperature rises, but the size and content of α-phase significantly decrease. It is noteworthy that transformation from α-Mg to β-Li is evident above 300 °C. The transformation of α-Mg to β-Li is carried by both spheroidization and internal precipitation of α-Mg phase.

3) Through comprehensive analysis of LA103Z alloy microstructure, α-Mg phase content map and hot processing maps at a strain of 0.7, the optimal processing windows of 300–350 °C/0.1–1 s^{-1} and 250 °C/0.1 s^{-1} are recommended as the optimal workable range for dual-phase Mg-Li alloy.

References

1 Zhang Jinlong, Lu Enhao, Zhu Jun *et al. Rare Metal Materials and Engineering*[J], 2021, 50(4): 1359

2 Edwin Eyram Klu, Jiang Jinghua, Bassiouny Saleh *et al. Rare Metal Materials and Engineering*[J], 2022, 51(2): 491

3 Xu D K, Wang B J, Li C Q *et al. Materials & Design*[J], 2015, 69: 124

4 Peng Xiang, Liu Wencai, Wu Guohua *et al. Journal of Materials Science & Technology*[J], 2022, 99: 193

5 Li Yong, Liu Junwei, Gao Wenliang *et al. Rare Metal Materials and Engineering*[J], 2022, 51(8): 2992

6 Chen Dexin, Kong Jing, Gui Zhenzhen *et al. Materials Letters*[J], 2021, 301: 130 358

7 Zhao Jun, Jiang Bin, Tang Aitao *et al. Materials Characteri-*

zation[J], 2020, 159: 110 041
8 Ji Hao, Peng Xiang, Zhang Xiaolong *et al. Journal of Alloys and Compounds*[J], 2019, 791: 655
9 Li Xiaoqiang, Ren Liang, Le Qichi *et al. Journal of Alloys and Compounds*[J], 2020, 831: 154 868
10 Yang Yan, Peng Xiaodong, Ren Fengjuan *et al. Journal of Materials Science & Technology*[J], 2016, 32(12): 1289
11 Zhou Gang, Yang Yan, Zhang Hanzhu *et al. Journal of Materials Science & Technology*[J], 2022, 103: 186
12 Ji Hao, Wu Guohua, Liu Wencai *et al. Journal of Alloys and Compounds*[J], 2021, 876: 160 181
13 Wei Guobing, Peng Xiaodong, Hadadzadeh Amir *et al. Mechanics of Materials*[J], 2015, 89: 241
14 Shalbafi M, Roumina R, Mahmudi R. *Journal of Alloys and Compounds*[J], 2017, 696: 1269
15 Sun Yuehua, Wang Richu, Ren Jian *et al. Materials Science and Engineering A*[J], 2019, 755: 201
16 Han J, Su X M, Jin Z H *et al. Scripta Materialia*[J], 2011, 64(8): 693
17 Xu T C, Peng X D, Qin J *et al. Journal of Alloys and Compounds*[J], 2015, 639: 79
18 Al-Samman T. *Acta Materialia*[J], 2009, 57(7): 2229
19 Qu Zhikun, Wu Ruizhi, Zhan Haibo *et al. Journal of Alloys and Compounds*[J], 2012, 536: 145
20 Su Zexing, Sun Chaoyang, Wang Mingjia *et al. Journal of Magnesium and Alloys*[J], 2022, 10(1): 281
21 Sakai T, Jonas J J. *Acta Metallurgica*[J], 1984, 32(2): 189
22 Askariani Seyed Alireza, Hasan Pishbin Seyed Mohammad. *Journal of Alloys and Compounds*[J], 2016, 688: 1058
23 Zhou Yucheng, Chen Zhaoyun, Ji Jinggan *et al. Journal of Alloys and Compounds*[J], 2019, 770: 540
24 Wang K, Li M Q. *Materials Science and Engineering A*[J], 2014, 600: 122
25 Wang Ke, Li Miaoquan. *Transactions of Nonferrous Metals Society of China*[J], 2016, 26(6): 1583
26 Sakai Taku, Belyakov Andrey, Kaibyshev Rustam *et al. Progress in Materials Science*[J], 2014, 60: 130
27 Rokni M R, Zarei Hanzaki A, Roostaei Ali A *et al. Materials & Design*[J], 2011, 32(4): 2339
28 Su Zexing, Wan Li, Sun Chaoyang *et al. Materials Characterization*[J], 2016, 122: 90
29 Liu Chongliang, Quan Gaofeng, Zhou Mingyang *et al. Rare Metal Materials and Engineering*[J], 2020, 49(8): 2591
30 Yang Liu, Guan Yingping, Duan Yongchuan *et al. Rare Metal Materials and Engineering*[J], 2020, 49(5): 1715
31 Zhao Haitao, Liu Guoquan, Xu Lei. *Materials Science and Engineering A*[J], 2013, 559: 262
32 Sun Yuehua, Wang Richu, Ren Jian *et al. Mechanics of Materials*[J], 2019, 131: 158
33 Liu Gang, Xie Wen, Hadadzadeh Amir *et al. Journal of Alloys and Compounds*[J], 2018, 766: 460
34 Sherby Oleg D, Taleff Eric M. *Materials Science and Engineering A*[J], 2002, 322(1): 89
35 Li Yi, Guan Yanjin, Liu Ya *et al. Journal of Materials Engineering and Performance*[J], 2022, 32: 2626
36 Shin Ilgyou, Carter Emily A. *Acta Materialia*[J], 2014, 64: 198
37 Wang Williamyi, Shang Shunli, Wang Yi *et al. Materials Research Letters*[J], 2014, 2(1): 29
38 Huang K, Logé R E. *Materials & Design*[J], 2016, 111: 548
39 Guo Fei, Liu Lei, Ma Yanlong *et al. Materials Science and Engineering A*[J], 2020, 772: 138 792
40 Zhang Qifei, Jin Miao, Zhang Yusen *et al. Materials Science and Engineering A*[J], 2022, 843: 143 110
41 Fei Pengfei, Qu Zhikun, Wu Ruizhi. *Materials Science and Engineering A*[J], 2015, 625: 169
42 Wang Cong, Liu Yunteng, Lin Tao *et al. Materials Characterization*[J], 2019, 157: 109 896
43 Prasad Y V R K, Gegel H L, Doraivelu S M *et al. Metallurgical Transactions A*[J], 1984, 15(10): 1883
44 Wei Zhen, Zhang Jinghuai, Bao Rirong *et al. Materials Science and Engineering A*[J], 2022, 846: 143 272

双相Mg-Li合金的$\alpha\rightarrow\beta$相变及热加工性能研究

冯英豪[1,2]，孙朝阳[1,2]，徐斯诺[1,2]，朱南洋[1,2]，王青磊[1,2]，王春晖[1,2]
(1. 北京科技大学 机械工程学院，北京 100083)
(2. 金属轻量化成形制造北京市重点实验室，北京 100083)

摘 要：在温度为250–400 ℃、应变速率为0.1–10 s^{-1}条件下进行了热压缩试验，研究了双相Mg-Li合金的热加工性能、显微组织演变和相组成。建立了整合加工和α-Mg相含量的最佳热加工窗口。结果表明，所建立的Arrhenius本构模型能够准确预测软化过程中的应力流动行为。通过对合金显微组织的观察，发现动态回复（DRV）、动态再结晶（DRX）和α-Mg相变是主要的软化机制。α-Mg相以球化和α-Mg相内析出的形式转变为β-Li相，尤其是在300 ℃以上相变现象显著。同时，DRX行为容易在β-Li相中发生，而在α-Mg相中会被抑制。基于动态材料模型和微观结构分析，获得最佳加工窗口：温度300–350 ℃/0.1–1 s^{-1}和温度250 ℃/0.1 s^{-1}。

关键词：Mg-Li合金；热变形行为；动态再结晶；加工优化；相变

作者简介：冯英豪，男，1992年生，博士生，北京科技大学机械工程学院，北京 100083，电话：010-62332261，E-mail：936631146@qq.com